

# Single-crystalline monolayer and multilayer graphene nano switches

Cite as: Appl. Phys. Lett. **104**, 113110 (2014); <https://doi.org/10.1063/1.4868869>

Submitted: 28 January 2014 . Accepted: 06 March 2014 . Published Online: 20 March 2014

Peng Li, Gaoshan Jing, Bo Zhang, Shota Sando, and Tianhong Cui



View Online



Export Citation



CrossMark

## ARTICLES YOU MAY BE INTERESTED IN

[Graphene cantilever beams for nano switches](#)

Applied Physics Letters **101**, 093111 (2012); <https://doi.org/10.1063/1.4738891>

[Wafer-size free-standing single-crystalline graphene device arrays](#)

Applied Physics Letters **105**, 083118 (2014); <https://doi.org/10.1063/1.4894255>

[Low pull-in voltage graphene electromechanical switch fabricated with a polymer sacrificial spacer](#)

Applied Physics Letters **105**, 033103 (2014); <https://doi.org/10.1063/1.4891055>

## Lock-in Amplifiers up to 600 MHz

starting at

\$6,210



Zurich Instruments

Watch the Video



AIP  
Publishing

## Single-crystalline monolayer and multilayer graphene nano switches

Peng Li,<sup>1,2</sup> Gaoshan Jing,<sup>1</sup> Bo Zhang,<sup>2</sup> Shota Sando,<sup>2</sup> and Tianhong Cui<sup>1,2,a)</sup>

<sup>1</sup>State Key Laboratory of Precision Measurement Technology and Instruments, Department of Precision Instruments, Tsinghua University, Beijing 100084, China

<sup>2</sup>Department of Mechanical Engineering, University of Minnesota, Minneapolis, Minnesota 55455, USA

(Received 28 January 2014; accepted 6 March 2014; published online 20 March 2014)

Growth of monolayer, bi-layer, and tri-layer single-crystalline graphene (SCG) using chemical vapor deposition method is reported. SCG's mechanical properties and single-crystalline nature were characterized and verified by atomic force microscope and Raman spectroscopy. Electro-mechanical switches based on mono- and bi-layer SCG were fabricated, and the superb properties of SCG enable the switches to operate at pull-in voltage as low as 1 V, and high switching speed about 100 ns. These devices exhibit lifetime without a breakdown of over 5000 cycles, far more durable than any other graphene nanoelectromechanical system switches reported. © 2014 AIP Publishing LLC. [<http://dx.doi.org/10.1063/1.4868869>]

Nanoelectromechanical systems (NEMS) are a rapidly growing research field for promising applications, for instance, NEMS switches, resonators, etc.<sup>1,2</sup> NEMS switches, with ideal zero off-current and excellent on-off current ratio,<sup>3</sup> could replace existing discrete metal-oxide-semiconductor (MOS) switches having intrinsic drawbacks as high power dissipation and strong short-channel effects.<sup>4</sup> In order to expand applications of NEMS switches, their moving parts should be further scaled down to reduce operation voltage and response time.<sup>2</sup> However, conventional bulk silicon based materials for NEMS switches become fragile when their thickness is reduced to nanoscale. Graphene, a two-dimensional honeycomb crystal material with sp<sup>2</sup>-bonded carbon atoms,<sup>5</sup> is predicted to be an excellent candidate for NEMS switches owing to its extremely small thickness, superb in-plane stiffness,<sup>6</sup> and very low mass.

Chemical vapor deposition (CVD) methods, especially on a copper substrate, have been widely used to grow large-area graphene monolayer film in recent years.<sup>7-9</sup> However, large area graphene film prepared by currently available growth methods is polycrystalline material,<sup>10,11</sup> and wafer-scale single-crystalline graphene (SCG) is far from being realized.<sup>12-15</sup> Because of grain boundaries inside graphene, most of graphene's electrical and mechanical properties degrade drastically, possibly having a detrimental effect on graphene based device performance.<sup>16-18</sup> For instance, polycrystalline graphene NEMS switches can only operate about 4-5 times before breakdown.<sup>2</sup> Although CVD growth of SCG grains was demonstrated,<sup>19,20</sup> SCG NEMS devices have not been reported so far, and how SCG can improve NEMS performance is unclear. In this Letter, we report a top-down approach combining low pressure chemical vapor deposition (LPCVD) and photolithography processes to obtain monolayer and multi-layer SCG NEMS switches with superb performance with pull-in voltage of about 1 V, switching speed of about 100 ns, and life time of over 5000 times.

LPCVD growth was carried out in a 2 in. quartz tube furnace with a mixture of methane and hydrogen at 1050 °C. Next, SCG was transferred onto a SiO<sub>2</sub>/Si substrate by PMMA (polymethyl methacrylate) assisted process. Finally, free-standing SCG NEMS switches were fabricated using microfabrication processes.

Prior to growth, a copper foil (25 μm thick, 99.8%, Alfa Aesar) was pre-treated by diluted nitric acid to remove native copper oxide surface on the copper substrate for a better growth. Because grain boundaries of a continuous polycrystalline graphene film are hardly visible under an optical microscope,<sup>21</sup> we stopped the growth before isolated graphene islands connected to each other to obtain SCG and avoid grain boundary generation during NEMS fabrication. Monolayer SCG growing on the copper foil with methane flowrate of 1.2 SCCM, 0.6 SCCM, and 0.12 SCCM is shown in Figures 1(a)-1(c), respectively. Most of monolayer SCG islands have star-like shapes and are uniformly distributed across the copper foil. Decreasing methane flow rate can

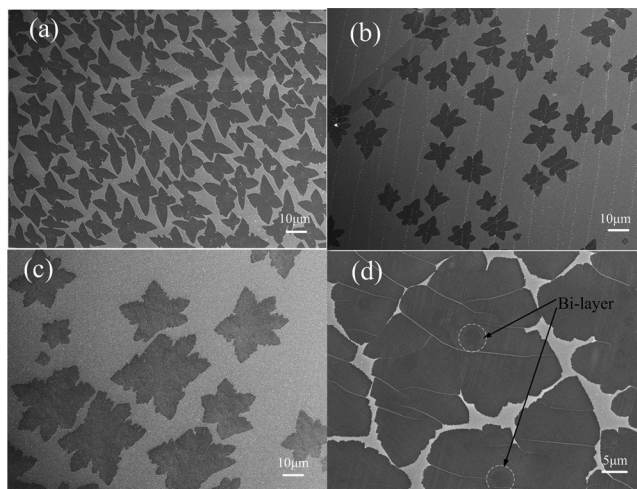


FIG. 1. (a) Scanning electron microscopy (SEM) image of SCGs on copper foil with methane flow rate of 1.2 SCCM. (b) SEM image of SCGs on copper foil with methane flow rate of 0.6 SCCM. (c) SEM image of SCGs on copper foil with methane flow rate of 0.12 SCCM. (d) Monolayer SCGs on copper with adlayer.

<sup>a)</sup> Author to whom correspondence should be addressed. Electronic mail: [tcui@me.umn.edu](mailto:tcui@me.umn.edu).

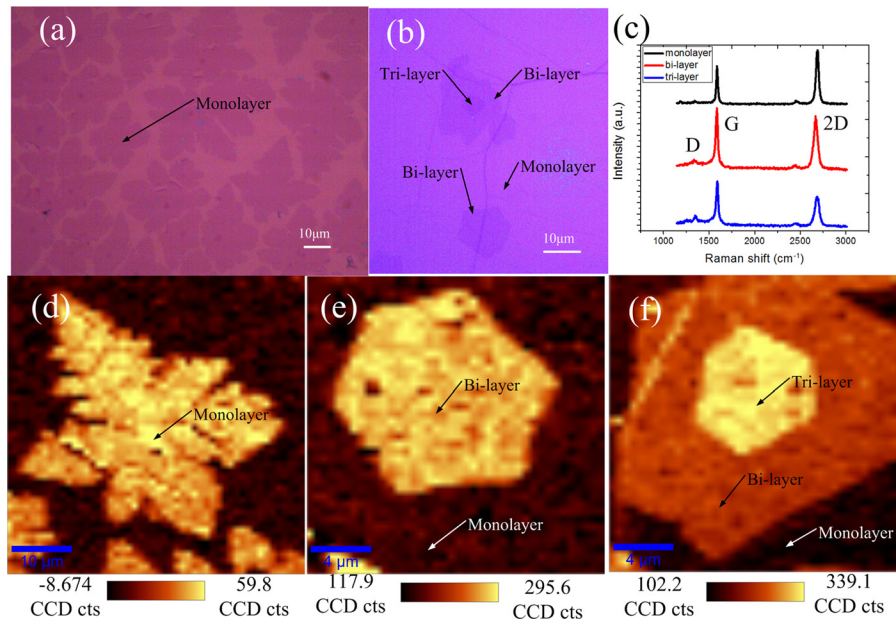


FIG. 2. (a) Optical view of monolayer SCGs on SiO<sub>2</sub>/Si substrate. (b) Optical view of bi-layer and tri-layer graphene on SiO<sub>2</sub>/Si substrate. (c) Raman spectra of mono-, bi-, and tri-layer graphene, respectively. (d) Raman G peak image of monolayer SCG. (e) Raman G peak image of bi-layer SCG. (f) Raman G Peak image of tri-layer graphene.

reduce nucleation density effectively, thus generate larger grain size. In addition, higher growth temperature and hydrogen/methane flow rate ratio can also result in larger grain sizes. Each SCG grain is over 10  $\mu\text{m}$ , large enough to fabricate NEMS switches. With longer growth time, adlayers were observed, as shown in Figure 1(d), which usually share the same nuclei with the first seed layer. A graphene adlayer has much smaller growth rate and smaller size than the first graphene layer. Unlike monolayer SCG, the second and third layer SCG are hexagonal shaped, with their edges macroscopically oriented predominantly parallel to zigzag directions.<sup>8</sup>

After LPCVD growth, SCG on the copper foil substrate was transferred onto a SiO<sub>2</sub>/Si substrate by PMMA assisted process,<sup>1</sup> and SCG physical properties were characterized by Raman mapping spectroscopy. In order to remove PMMA residues, the sample was heated up to 300  $^{\circ}\text{C}$  at low pressure for 3 h.<sup>22</sup> Monolayer SCGs on a SiO<sub>2</sub>/Si substrate were shown in Figure 2(a). In Figure 2(b), the darker color demonstrated the adlayer inside a graphene film. Number of graphene layers and defects inside graphene were verified by 2D/G peak intensity ratio and D peak intensity, respectively. Bi- and tri-layer have a broader and lower 2D band with respect to monolayer graphene, as shown in Figure 2(c).

Mono-, bi-, and tri-layer SCG were shown in Figures 2(d)–2(f), and hexagonal shape of adlayers was demonstrated in Figure 2(f). Negligibly small D peak (the intensity ratio of D band to G band is less than 5%) over most of the area within a graphene grain indicates low-defect and single-crystal nature of our sample, since grain boundary could increase D peak intensity.

Free-standing SCG devices were fabricated with micro-fabrication processes. First, star-like shaped monolayer SCG and hexagonal shaped bi-layer SCG were etched into rectangular beams by O<sub>2</sub> plasma dry etching. The electrode fabrication involves photolithography, Cr (10 nm)/Au (100 nm) electron-beam evaporation, and metal lift-off. One important thing should be emphasized on this process is that we designed graphene nuclei located beneath contact electrodes

instead of on the beam, because graphene nuclei have relatively more defects than other parts of graphene.<sup>9,23</sup> Buffered oxidize etchant (BOE) was applied to etch SiO<sub>2</sub> beneath graphene and release the free-standing structure, followed by critical point drying to avoid stiction. We fabricated the SCG beams with different lengths, which range between 1–5  $\mu\text{m}$ . The width of the beam is about 2  $\mu\text{m}$ , and the gap between SCG and substrate is 300 nm.

A graphene beam array derived from one large monolayer SCG and bi-layer SCG were shown in Figures 3(a) and 3(b), respectively. As shown in Figure 3(c), D peak intensity inside the SCG beam is slightly larger than that of SCG grains, indicating minor defects generated during device fabrication process. As shown in Figure 3(e), the 2D/G peak intensity ratio image demonstrates good uniformity of the beam thickness.

Mechanical properties of SCG beams were investigated by atomic force microscopy (AFM). Dynamic mode was chosen for high-resolution topographic imaging, as shown in Figure 4(a), to minimize the tip's shear interaction with the delicate structure to avoid damage. During indentation, the relationship among graphene beam displacement,  $Z_{beam}$ , piezo stage movement beneath sample,  $Z_{piezo}$ , and AFM cantilever deflection,  $Z_{afm}$ , is given by

$$Z_{beam} = Z_{piezo} - Z_{afm}. \quad (1)$$

Figure 4(b) showed four representative force curves. One curve obtained on the rigid Si substrate was used as a reference to calibrate the sensitivity of the cantilever deflection measurement. The other three curves were derived by indenting 3 different locations on beam described in Figure 4(a) as spot 1, 2, and 3, respectively. Lesser slope corresponds to reduced stiffness in a force curve. The stiffness reaches a minimum at the center with respect to the long beam axis, but a maximum with respect to the short beam axis (saddle shaped stiffness distribution). In addition, force curves imply the nonlinear property of a two-end-fixed graphene beam. Based on the force curves derived from

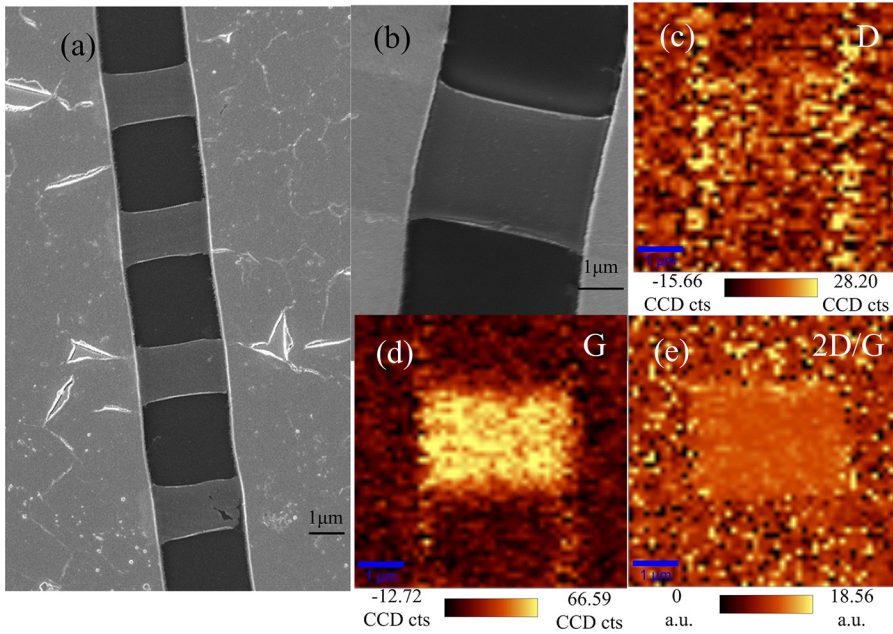


FIG. 3. (a) SEM image of graphene beam arrays from 1 monolayer SCG. (b) SEM image of bilayer SCG beam. (c) Raman D peak image of a suspended monolayer SCG. (d) Raman G peak image of a suspended monolayer SCG. (e) Raman 2D/G peak image of a suspended monolayer SCG.

different graphene beams we tested, Young's modulus of  $0.8 \pm 0.09$  TPa was deduced. The deduction method is similar to those reported previously.<sup>24,25</sup> This value is comparable to that of mechanically exfoliated graphene,<sup>6</sup> indicating high quality and single-crystalline nature of our samples.

Electromechanically actuated NEMS switches based on SCG in different thicknesses were investigated according to three parameters: (1) Pull-in voltage, (2) life time, and (3) switching speed. Top graphene film can be pulled to be in contact with the conductive substrate when applying a DC voltage. Once applied bias is larger than a threshold voltage, pull-in voltage, a sharp increase of the current will be observed which will indicate the switch is turned on. On contrary, the contact will be broken by an elastic force after the bias is removed. The pull-in voltage is given by

$$V_{pull-in} = \sqrt{\frac{8kg_0^3}{27\varepsilon A}}, \quad (2)$$

where  $k$  is the spring constant of the beam,  $g_0$  is the gap between beam and substrate,  $\varepsilon$  is the vacuum permittivity, and  $A$  is the size of suspended graphene beam over lower electrodes. Thinner beam is softer with smaller spring constant,  $k$ , thus the pull-in voltage is smaller. Pull-in voltage of monolayer SCG switch tested was about 1 V, while that of bi-layer SCG was about 1.5 V (Figure 4(c)). This value is much smaller than conventional MEMS switches, and it is compatible with MOS circuit requirements.<sup>2</sup> The Young's modulus of SCG deduced from the pull-in voltage is about 0.9 TPa. We assume the different deflection region is responsible for the difference between two Young's modulus values deduced. During AFM indentation, the SCG has very small deflection, while during switching an SCG beam has relatively larger deflection.

Life time limited by fracture failure is the bottleneck of graphene actuators (resonators<sup>1</sup> and switches<sup>2</sup>). Without the influence of grain boundary, our switches show longer life time than that of other graphene NEMS switches reported in literature.<sup>26</sup> Our mono- and bi-layer SCG devices switched 5000 times without failure, as shown in Figure 4(c), while polycrystalline graphene beam is reported to operate only 4–5 times due to mechanical grain boundary defect,<sup>2</sup> and graphene beam from mechanical exfoliation can operate 500 times before breakdown.<sup>26</sup>

Switching speed is another important parameter. For electromechanically actuated switches, switching time consists of response time, which is the time required to overcome mechanical inertia, and rise time of the voltage pulse due to charging capacitance. The switching time,  $t$ , is given by

$$t = \frac{3.67V_{pull-in}}{2\pi f_0 V}, \quad (3)$$

where  $V$  is the step function voltage, and  $f_0$  is the first order resonant frequency of beam. In general, conventional MEMS/NEMS has a switching time in the microsecond

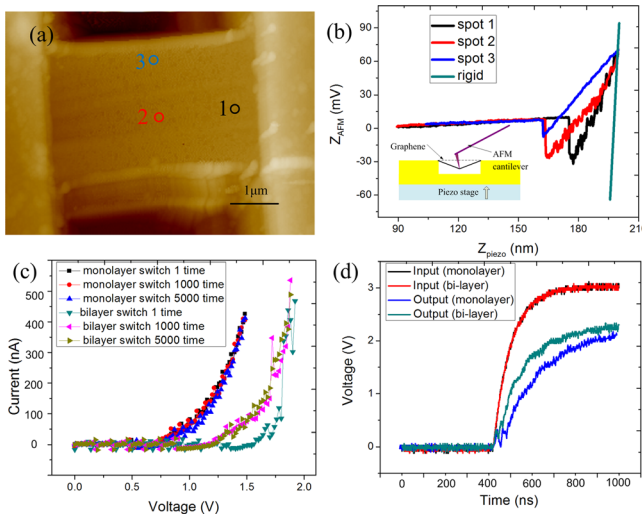


FIG. 4. (a) AFM topographic image of a suspended monolayer SCG beam. (b) Force curves from 3 different spots on the beam described in a. The force curve derive from rigid Si surface is used as a calibration curve. (c) I-V curves of monolayer SCG switch and bi-layer SCG switch, respectively. (d) The input signal and output signal of monolayer SCG switch and bi-layer SCG switch, respectively.

regime.<sup>3</sup> However, the extremely low mass density and high Young's modulus of graphene result in a high resonant frequency, showing possible operation in nanosecond regime. A step function was applied to the NEMS switch input terminal, and the output signal was measured. Switching speed of our graphene switch was characterized by applying a step signal to the device input terminals, while the output signal was measured concurrently, as shown in Figure 4(d). The time difference between these two signals is in the order of 100 ns, the delay time, indicating an upper bound of the intrinsic switching speed of the switch. Due to higher resonant frequency, bi-layer SCG shows faster switching speed than monolayer SCG switch.

In conclusion, we used LPCVD method to grow mono-, bi-, and tri-layer SCG. Raman characterization identifies their number of layers and demonstrates the low-defect and single-crystal nature of our samples. Young's modulus derived by AFM indentation indicates the mechanical properties of our graphene sample is comparable to mechanically exfoliated graphene. Mono- and bi-layer SCG NEMS switches were fabricated to demonstrate the effectiveness of our method. Monolayer SCG shows lower pull-in voltage, while bi-layer shows faster switching speed. The outstanding mechanical properties of SCG enable the switches to operate at a very low pull-in voltage and a very fast switching speed. The devices exhibit lifetime of over 5000 cycles without a breakdown, better than other graphene NEMS switches reported. The results presented here suggest that CVD SCG is an excellent candidate for NEMS switches.

The authors acknowledge the assistance of fabrication and characterization from Minnesota Nano Center and Characterization Facility at the University of Minnesota. The authors also thank Dr. Greg Haugstad for the assistance of graphene AFM indentation measurement.

<sup>1</sup>A. M. van der Zande, R. A. Barton, J. S. Alden, C. S. Ruiz-Vargas, W. S. Whitney, P. H. Q. Pham, J. Park, J. M. Parpia, H. G. Craighead, and P. L. McEuen, *Nano Lett.* **10**, 4869 (2010).

<sup>2</sup>K. M. Milaninia, M. A. Baldo, A. Reina, and J. Kong, *Appl. Phys. Lett.* **95**, 183105 (2009).

<sup>3</sup>I. J. Cho, T. Song, S. H. Baek, and E. Yoon, *IEEE Trans. Microwave Theory Tech.* **53**, 2450 (2005).

<sup>4</sup>R. Badzey, G. Zolfagharkhani, A. Gaidarzhy, and P. Mohanty, *Appl. Phys. Lett.* **85**, 3587 (2004).

<sup>5</sup>K. S. Novoselov, A. K. Geim, S. V. Morozov, D. Jiang, Y. Zhang, S. V. Dubonos, I. V. Grigorieva, and A. A. Firsov, *Science* **306**, 666 (2004).

<sup>6</sup>C. Lee, X. Wei, J. W. Kysar, and J. Hone, *Science* **321**, 385 (2008).

<sup>7</sup>X. Li, W. Cai, J. An, S. Kim, J. Nah, D. Yang, R. Piner, A. Velamakanni, I. Jung, E. Tutuc, S. K. Banerjee, L. Colombo, and R. S. Ruoff, *Science* **324**, 1312 (2009).

<sup>8</sup>Q. Yu, L. A. Jauregui, W. Wu, R. Colby, J. Tian, Z. Su, H. Cao, Z. Liu, D. Pandey, D. Wei, T. F. Chung, P. Peng, N. P. Buisinger, E. A. Stach, J. Bao, S. S. Pei, and Y. P. Chen, *Nature Mater.* **10**, 443 (2011).

<sup>9</sup>X. Li, C. W. Magnuson, A. Venugopal, J. An, J. W. Suk, B. Han, M. Borysiak, W. Cai, A. Velamakanni, Y. Zhu, L. Fu, E. M. Vogel, E. Voelkl, L. Colombo, and R. S. Ruoff, *Nano Lett.* **10**, 4328 (2010).

<sup>10</sup>K. S. Kim, Y. Zhao, H. Jang, S. Y. Lee, J. M. Kim, K. S. Kim, J. H. Ahn, P. Kim, J. Y. Choi, and B. H. Hong, *Nature* **457**, 706 (2009).

<sup>11</sup>L. Gao, W. Ren, H. Wu, L. Jin, Z. Wang, T. Ma, L. P. Ma, Z. Zhang, Q. Fu, L. M. Peng, X. Bao, and H. M. Cheng, *Nat. Commun.* **3**, 699 (2012).

<sup>12</sup>Y. Hao, M. S. Bharathi, L. Wang, Y. Liu, H. Chen, S. Nie, X. Wang, H. Chou, C. Tan, B. Fallahazad, H. Ramanarayan, C. W. Magnuson, E. Tutuc, B. I. Yakobson, K. F. McCarty, Y. W. Zhang, P. Kim, J. Hone, L. Colombo, and R. S. Ruoff, *Science* **342**, 720 (2013).

<sup>13</sup>S. Chen, H. Ji, H. Chou, Q. Li, H. Li, J. W. Suk, R. Piner, L. Liao, W. Cai, and R. S. Ruoff, *Adv. Mater.* **25**, 2062 (2013).

<sup>14</sup>Z. Yan, J. Lin, Z. W. Peng, Z. Z. Sun, Y. Zhu, L. Li, C. S. Xiang, E. L. Samuel, C. Kittrell, and J. M. Tour, *ACS Nano* **7**, 2872 (2013).

<sup>15</sup>Y. A. Wu, Y. Fan, S. Speler, G. L. Creeth, J. T. Sadowski, K. He, A. W. Robertson, C. S. Allen, and J. H. Warner, *ACS Nano* **6**, 5010 (2012).

<sup>16</sup>G. H. Lee, R. C. Cooper, S. J. An, S. Lee, A. van der Zande, N. Petrone, A. G. Hammerberg, C. Lee, B. Crawford, W. Oliver, J. W. Kysar, and J. Hone, *Science* **340**, 1073 (2013).

<sup>17</sup>H. I. Rasool, C. Ophus, W. S. Klug, A. Zettl, and J. K. Gimzewski, *Nat. Commun.* **4**, 2811 (2013).

<sup>18</sup>K. Yagi, A. Yamada, K. Hayashi, N. Harada, S. Sato, and N. Yokoyama, *Jpn. J. Appl. Phys.* **52**, 110106 (2013).

<sup>19</sup>Y. Xue, B. Wu, L. Jiang, Y. Guo, L. Huang, J. Chen, J. Tan, D. Geng, B. Luo, W. Hu, G. Yu, and Y. Liu, *J. Am. Chem. Soc.* **134**, 11060 (2012).

<sup>20</sup>A. T. Murdock, A. Koos, T. Ben Britton, L. Houben, T. Batten, T. Zhang, A. J. Wilkinson, R. E. Dunin-Borkowski, C. E. Lekka, and N. Grobert, *ACS Nano* **7**, 1351 (2013).

<sup>21</sup>D. L. Duong, G. H. Han, S. M. Lee, F. Gunes, E. E. Kim, S. T. Kim, H. Kim, Q. H. Ta, K. P. So, S. J. Yoon, S. J. Chae, Y. W. Jo, M. H. Park, S. H. Chae, S. C. Lim, J. Y. Choi, and Y. H. Lee, *Nature* **490**, 235 (2012).

<sup>22</sup>Z. Cheng, Q. Zhou, C. Wang, Q. Li, C. Wang, and Y. Fang, *Nano Lett.* **11**, 767 (2011).

<sup>23</sup>W. Wu, L. A. Jauregui, Z. Su, Z. Liu, J. Bao, Y. P. Chen, and Q. Yu, *Adv. Mater.* **23**, 4898 (2011).

<sup>24</sup>C. Gomez-Navarro, M. Burghard, and K. Kern, *Nano Lett.* **8**, 2045 (2008).

<sup>25</sup>I. W. Frank, D. M. Tanenbaum, A. M. Van der Zande, and P. L. McEuen, *J. Vac. Sci. Technol. B* **25**, 2558 (2011).

<sup>26</sup>Z. W. Shi, H. L. Lu, L. C. Zhang, R. Yang, Y. Wang, D. H. Liu, H. M. Guo, D. X. Shi, H. J. Gao, E. G. Wang, and G. Y. Zhang, *Nano Res.* **5**, 82 (2012).